ADVANCED ELECTRONIC MATERIALS
Open Access
www.advelectronicmat.de

Improved Performance of Hf_xZn_yO-Based RRAM and its Switching Characteristics down to 4 K Temperature

*Jun Lan, Zhixiong Li, Zhenjie Chen, Quanzhou Zhu, Wenhui Wang, Muhammad Zaheer, Jiqing Lu, Jinxuan Liang, Mei Shen, Peng Chen, Kai Chen, Guobiao Zhang, Zhongrui Wang, Feichi Zhou, Longyang Lin, and Yida Li**

The search for high-performance resistive random-access memory (RRAM) devices is essential to pave the way for highly efficient non-Von Neumann computing architecture. Here, it is reported on an alloying approach using atomic layer deposition for a Zn-doped HfO_x-based resistive random-access memory (HfZnO RRAM), with improved performance. As compared with HfO_x RRAM, the HfZnO RRAM exhibits reduced switching voltages (>20%) and switching energy (>3×), as well as better uniformity both in voltages and resistance states. Furthermore, the HfZnO RRAM exhibits stable retention exceeding 10 years, as well as write/erase endurance exceeding 10^5 cycles. In addition, excellent linearity and repeatability of conductance tuning can be achieved using the constant voltage pulse scheme, achieving ≈90% accuracy in a simulated multi-layer perceptron network for the recognition of modified national institute of standards and technology database handwriting. The HfZnO RRAM is also characterized down to the temperature of 4 K, showing functionality and the elucidation of its carrier conduction mechanism. Hence, a potential pathway for doped-RRAM to be used in a wide range of temperatures including quantum computing and deep-space exploration is shown.

1. Introduction

To facilitate more extensive implementation of next-generation in-memory-computing systems, resistive random-access memory (RRAM) is widely considered to be one of the most promising building blocks.[1–7] In recent years, metal-oxides-based RRAMs have been implemented in an artificial neural network with considerable success,[8–11] but with performance metrics that can be further improved. In addition, with the recent rise of quantum applications, the use of resistive memory (e.g., RRAM) for storage or computation under cryogenic conditions starts to attract research interests. However, currently, the application of RRAM under cryogenic conditions still meets unexpected issues like poor endurance and device uniformity, lacks study on how efficiently it can operate in an environment lacking in thermal energy.[12–17] Hence, there is an urgent need to further develop RRAM with consistent performance down to cryogenic temperatures for widespread applications in emerging industries.

Among various metal-oxides, Hafnium oxide stands out as one of the most commonly used RRAM resistive switching (RS) layer due to its superior complementary metal oxide semiconductor compatibility and decent switching characteristics.[18–20] In the deposition process, Hafnium oxide is usually deposited using the atomic layer deposition (ALD) approach, which has the additional advantage of higher precision in controlling the atomic composition, roughness, and thickness of the switching layer. However, Hafnium oxide deposited by ALD tends to have a low concentration of defects, which may lead to high forming/switching voltage as well as abrupt switching behavior. Therefore, finding a way to introduce more defects/impurities into the RS layer may be an effective way to achieve performance enhancement. Advanced process technique such as doping/mixing is one of the promising approaches, as it has been proven to allow more superior control of device characteristic and improve device performance.[21–23]

J. Lan, Z. Li, Z. Chen, Q. Zhu, W. Wang, M. Zaheer, J. Lu, P. Chen, K. Chen, G. Zhang, F. Zhou, L. Lin, Y. Li
School of Microelectronics
Southern University of Science and Technology
Shenzhen 518055, P. R. China
E-mail: liyd3@sustech.edu.cn

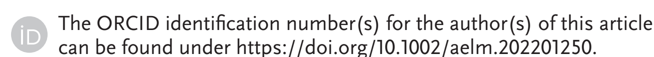
The ORCID identification number(s) for the author(s) of this article can be found under https://doi.org/10.1002/aelm.202201250.

© 2023 The Authors. Advanced Electronic Materials published by Wiley-VCH GmbH. This is an open access article under the terms of the Creative Commons Attribution License, which permits use, distribution and reproduction in any medium, provided the original work is properly cited.

DOI: 10.1002/aelm.202201250

Z. Li
Shenzhen Longsys Electronics Co., Ltd
Shenzhen 518057, P. R. China

J. Liang, M. Shen
SUSTech Academy for Advanced Interdisciplinary Studies
Southern University of Science and Technology
Shenzhen 518055, P. R. China

Z. Wang
Department of Electrical and Electronic Engineering
The University of Hong Kong
Hong Kong, SAR 999077, P. R. China

ADVANCED ELECTRONIC MATERIALS
Open Access
www.advelectronicmat.de

2199160x, 2023, 3, Downloaded from https://onlinelibrary.wiley.com/doi/10.1002/aelm.202201250 by University of Hong Kong, Wiley Online Library on [26/12/2023]. See the Terms and Conditions (https://onlinelibrary.wiley.com/terms-and-conditions) on Wiley Online Library for rules of use; OA articles are governed by the applicable Creative Commons License

Many attempts have been studied to investigate the potential mechanism of doping and, thus, to pursue better performance including voltages, stability, multi-states storage capability as well as synaptic behavior.[24–30] Lübben et al. systematically studied how the material purity, chemistry, and concentrations of intrinsic/extrinsic doping influence devices' kinetics and, thus, affect the performance and functionalities.[24] Raeis-Hosseini et al. introduced Zr in TaO_x-based RRAM to achieve stable bipolar resistive switching properties with reliable endurance and retention, since the doped Zr can enhance the stability of the conductive filament.[25] Zhao et al. doped Li into SiO_2 by co-sputtering to form a Li_xSiO_y-based RRAM so that fast programming speed (<10 ns) and reliable endurance(10^9 cycles) were demonstrated.[26] Ismail et al. demonstrated $HfAlO_x$ alloy-based memristor by using ALD to prepare the RS layer, achieving a forming-free switching behavior with a high current ON/OFF ratio, highly controllable conductance,[27] and better synaptic characteristics.[28,29] Zhang et al. introduced the Hf element into ZnO by co-sputtering to solve the instability issue of ZnO-based RRAM and, thus, achieved remarkable 10^8 pulse endurance as well as an ON/OFF ratio of 2 order.[30] However, among the existing works, several studies focused on Zn-doped HfO film, and none of them looked into the use in RRAM. Although some doping works of Hf-doped ZnO film[31,32] were investigated,[30] few works focused on the study of Zn-doped HfO RRAM. ZnO deposited by ALD is an n-type semiconductor that contains a high concentration of native defects such as oxygen vacancies and zinc interstitials.[33] However, the RRAMs based on pure ZnO usually suffer from instability and performance degradation.[34,35] Instead, taking advantage of the stable switching characteristics of hafnium oxide, doping ZnO, which contains more defects, may provide another effective solution to achieve performance improvement of the device in hafnium/zinc oxide doping systems.

Hence, in this work, we propose a Zn-doped HfO_x (HfZnO) RRAM deposited by ALD at a relatively low temperature of 200 °C. The ALD process provides us with highly controllable composition and thickness uniformity. As compared to HfO_x-based RRAM prepared using ALD, HfZnO RRAM exhibits lower forming/set/reset voltages (1.77/0.95/–1.05 V vs. 3.41/1.25/–1.23 V), and consequently 3× lower switching energy (19 pJ). This can be attributed to weaker Zn—O bonds leading to a larger content of defects as elucidated from our X-ray photoelectron spectroscopy (XPS) analysis. In addition, the stability, as well as multiple states modulation, was also investigated. Finally, we investigated the switching behavior of HfZnO RRAM down to 4 K, where temperature dependence of the switching voltages and resistance were studied. The carrier conduction mechanism of the HfZnO RRAM is analyzed to provide a better understanding of such a class of RRAM, thus paving a pathway for its use in cryogenic conditions.

2. Results and Discussion

The proposed RRAMs were fabricated with a typical cross-point structure using the same process flow except for the RS layer, as shown in **Figure 1**a,b. Both of bottom electrode (BE) and top electrode (TE) were composed of Ti/Pt with the thickness of 5/20 and 8/20 nm, respectively. The metal oxide was selected as the RS layer of RRAM, which was prepared by ALD. Four RS layers with ALD cycle ratios (ZnO: HfO_2) of 0:1, 1:1, 1:3, and

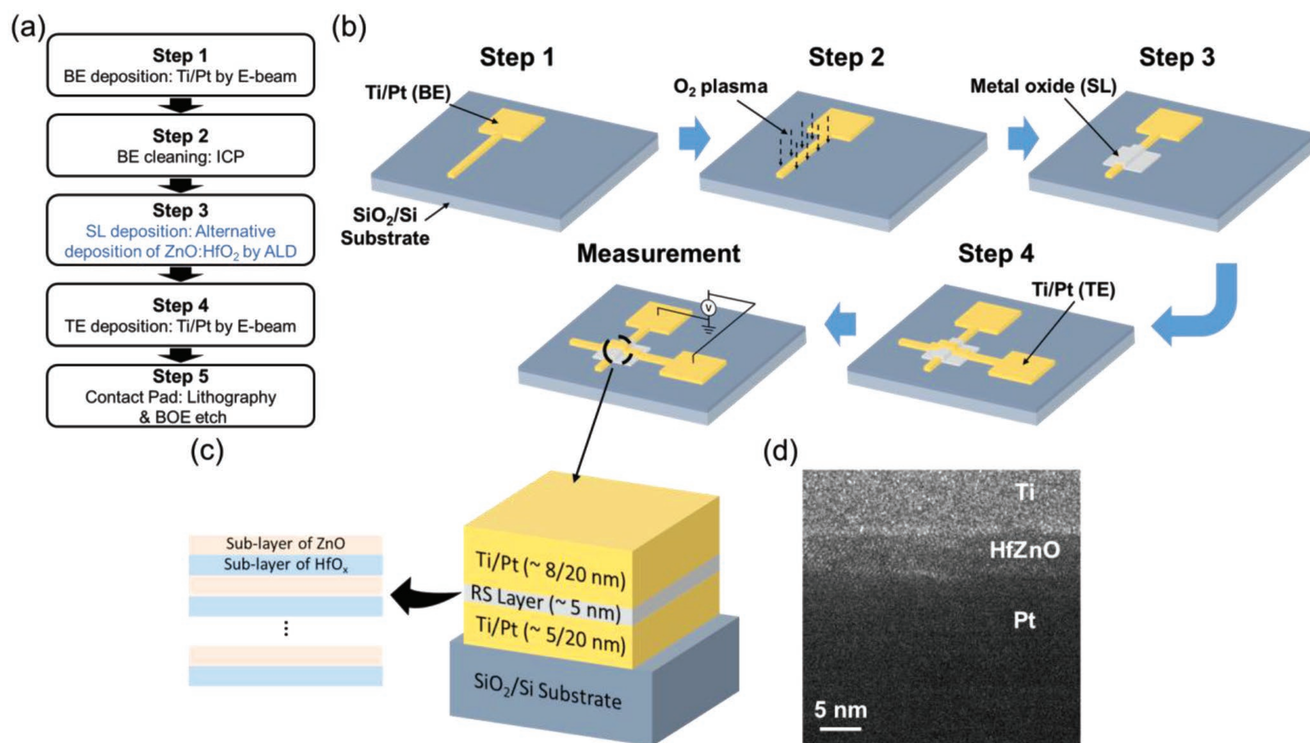

Figure 1. a) Fabrication process flow and b) corresponding schematic of fabrication. c) Cross-sectional illustration of HfZnO RRAM and d) TEM image.

 © 2023 The Authors. Advanced Electronic Materials published by Wiley-VCH GmbH

ADVANCED ELECTRONIC MATERIALS Open Access
www.advelectronicmat.de

2199160x, 2023, 3, Downloaded from https://onlinelibrary.wiley.com/doi/10.1002/aelm.202201250 by University of Hong Kong, Wiley Online Library on [26/12/2023]. See the Terms and Conditions (https://onlinelibrary.wiley.com/terms-and-conditions) on Wiley Online Library for rules of use; OA articles are governed by the applicable Creative Commons License

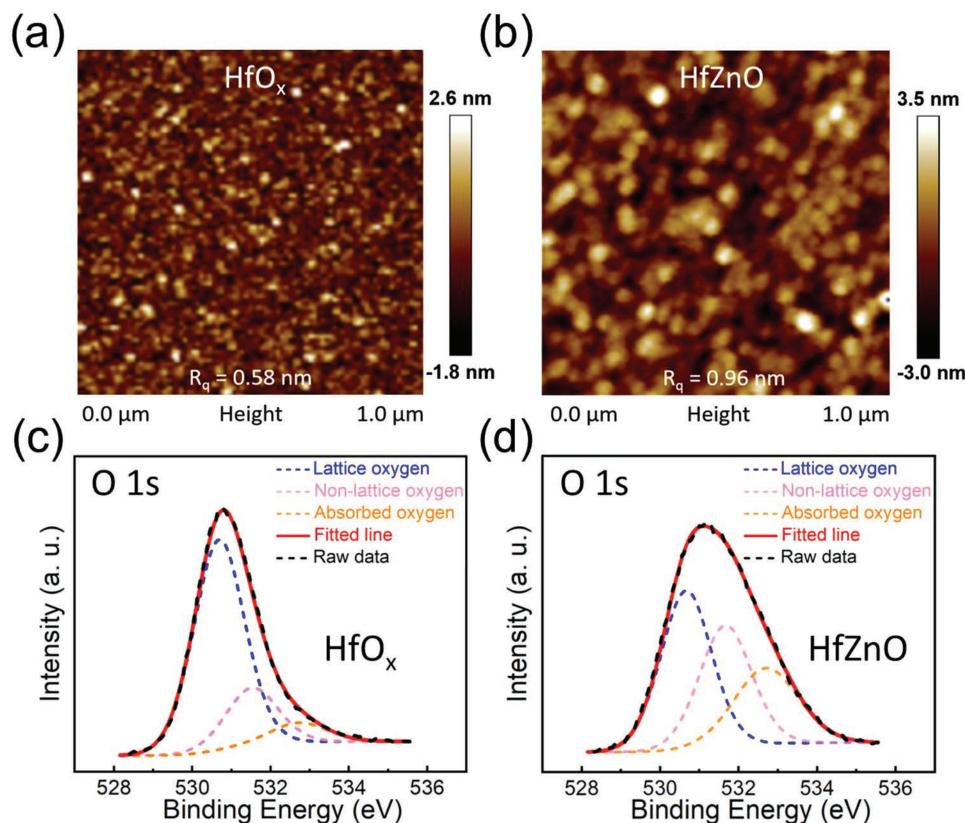

Figure 2. Morphology analysis of AFM for a) HfO_x and b) HfZnO. Material characterization using XPS for c) HfO_x and d) HfZnO.

1:0 were prepared, with all having a thickness ≈5 nm. Details of the ALD process is given in Table S1 (Supporting Information) as well as in the Experimental Section. Illustrations of HfZnO RRAM and corresponding transmission electron microscope (TEM) image are shown in Figure 1c,d.

Atomic force microscope (AFM) and XPS were performed for the morphology analysis of both as-deposited HfO_x and HfZnO film on BE. The AFM images of both films were carried out as shown in **Figure 2**a,b with the scanning range of 1×1 µm^2. As compared to HfO_x film, larger white tips are observed in the HfZnO film, consequently resulting in an overall rougher surface (0.58 nm vs. 0.96 nm). The larger white tips could be related to localized nano-crystallization of the film, as a result of the introduction of ZnO.[33]

To analyze the composition of the RS layer of two types of devices, HfO_x film and HfZnO film were characterized by XPS, respectively. The atomic ratios of Zn: Hf: O for HfO_x and HfZnO film are extracted from the XPS spectra to be 0:38.5:61.5 and 9.7:24.6:65.7, respectively. In reference to previous literature, the XPS of the O1s spectra can be deconvoluted into three components including lattice oxygen (LO), non-lattice oxygen (N-LO), and absorbed oxygen, based on the position of referenced binding energy.[36–40] As shown in Figure 2c,d, the same approach was used to deconvolute the XPS O1s spectra of both films into three peaks. The lower binding energy peak located at ≈530.7 eV (blue), with FWHM of 1.6 eV, corresponds to the LO or metal-oxide (MO), while the higher binding energy peak centered at ≈532.7 eV (orange) corresponds to the absorbed oxygen like hydroxyl groups (–OH), which might come from the intermediate groups in ALD reactions. The medium binding energy peak located at ≈531.6 eV (red), with FWHM of 1.6 eV, corresponds to the N-LO, which can be assigned to the oxygen defects in the oxygen-deficient region.[38–40] For these three components, the density of the peak representing N-LO in the HfZnO film is significantly higher than that of HfO_x film (height ratio of N-LO: LO [HfZnO: HfO_x = 76%:27%]) while the density of the peak representing LO of HfZnO film is much lower. This indicates that the strength of the M—O bond in the pristine HfZnO films is weaker while possessing a higher concentration of oxygen defects. In addition, as presented in Figure 2d, the concentration of absorbed oxygen at the highest binding energy of ≈532.7 eV significantly increases, which indicates adding ZnO might also influence the role of moisture,[41] for example, bringing additional moisture into the RS layer. Ambient moisture has been proven to affect the performance of the device, since water molecules as well as protons under moisture condition may be directly involved in the redox processes leading to additional ionic species in the oxide layer so as to be beneficial to the forming process, the switching voltages, and determine the high resistance state.[42–44] Combining with the observation of higher defects concentration in the HfZnO film, it is reasonable to assume that the introduction of ZnO might be beneficial for the electroforming as well as easier write/erase operations.

For further verification, the DC electrical characteristics of HfO_x RRAM and HfZnO RRAM were compared at

 © 2023 The Authors. Advanced Electronic Materials published by Wiley-VCH GmbH

2199160x, 2023, 3, Downloaded from https://onlinelibrary.wiley.com/doi/10.1002/aelm.202201250 by University of Hong Kong, Wiley Online Library on [26/12/2023]. See the Terms and Conditions (https://onlinelibrary.wiley.com/terms-and-conditions) on Wiley Online Library for rules of use; OA articles are governed by the applicable Creative Commons License

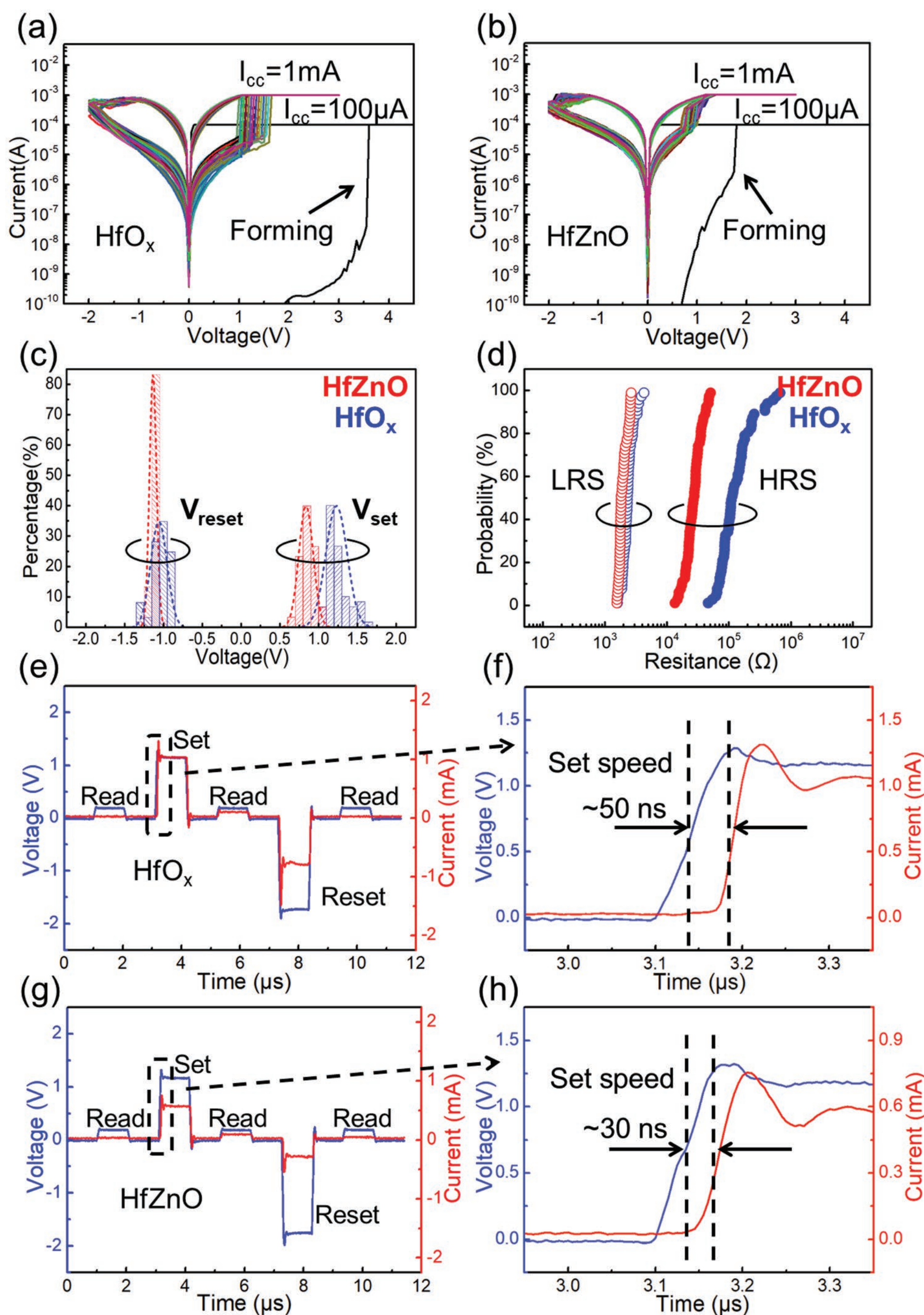

Figure 3. I–V curves of a) HfO_x and b) HfZnO RRAM under a CC of 1 mA (CC for electroforming is 100 µA). Distribution of the c) set/reset voltage, and d) low/high resistance states (LRS/HRS) extracted from 60 consecutive switching cycles for C2C analysis. Switching process under pulsing conditions and switching speeds for e,f) HfO_x RRAM and g,h) HfZnO RRAM. Both devices were tested using voltage pulses of 1 µs width, and switching speeds were extracted at FWHM.

room temperature, as shown in **Figure 3**. Figure 3a,b show the I–V curves of the HfO_x and HfZnO RRAM, respectively, including the electroforming process and 60 consecutive normal switching cycles. The compliance current (CC), which is to mimic the transistor, during electroforming was limited to 100 µA to prevent the RRAM from irreversible damage.[45,46] During the normal switching cycle, a compliance current of 1 mA was used. From Figure 3a,b, we can observe that HfZnO RRAM shows lower switching voltage, better cycle-to-cycle uniformity as well as more gradual switching behavior, which is beneficial in avoiding current overshoot and damage of RRAM during the switching process. Meanwhile, it should be noted that the ON/OFF ratio of HfZnO RRAM is smaller than that of HfO_x RRAM due to higher current of HRS. This is a trade-off

 © 2023 The Authors. Advanced Electronic Materials published by Wiley-VCH GmbH

since ambient moisture brought by adding ZnO would not only assist the forming/switching process but also decrease the resistance of high resistance states (HRS) due to more defects in the RS layer.[42,43] A dry annealing-treatment process might be one way to alleviate the effect of ambient moisture, from the device point-of-view.[41] Besides, from the system point-of-view, since the ON/OFF ratio of a single device is one of the factors affecting the integration of an array,[47] the HfZnO RRAM in an array could be paired with a selector (e.g., transistor) that can effectively inhibit the leakage current (i.e., current of HRS)[45] when the cell is not selected.

To quantify the observation from I–V curves, cycle-to-cycle variation (C2C) of voltages from the measurement of Figure 3a,b was shown in Figure 3c with the distribution histograms, as well as the Gaussian fitting curve of each histogram. After measuring 60 consecutive switching cycles, it can be seen from Figure 3c that although the average reset voltage of HfZnO RRAM is a little larger than that of HfO_x RRAM, the set voltage was reduced from 1.23 to 0.84 V, which is a 32% reduction from that of HfO_x RRAM, while the distribution of set and reset voltages are tighter as well (σ/μ value of set/reset voltages: 3.99%/10.05% vs. 11.11%/11.16%), as compared to that of HfO_x RRAM. As indicated in Figure 3d, the resistance of HfZnO RRAM also shows a tighter distribution, with the σ/μ value of 16.46% and 31.19% for low (LRS) and HRS respectively, as compared to that of HfO_x RRAM (22.66% for LRS, 80.32% for HRS). This indicates the advantages of the doping approach for uniformity improvement, as the immobility of dopants could mitigate switching stochasticity.[23]

For further investigation of influence by the introduction of ZnO, the devices based on four RS layers with varying HfO_x and ZnO ALD cycle ratios were prepared. It should be noted that among these type of devices, the pure ZnO-based device shows no switching behavior, as shown in Figure S1 (Supporting Information). This is likely due to excessive defects in the ZnO film, since ZnO deposited by ALD is more conductive due to the presence of defects and impurities in the ZnO crystal,[33] and our film thickness is relatively thin (≈5 nm). For the rest of the devices, the DC switching characteristics and cumulative distribution plot over 20 individual devices are presented in Figure S2 (Supporting Information). We can observe a trend of lower forming and operating voltages when the ALD cycle ratio of ZnO in the RS layer increases. This is further indicated in XPS O1s spectra results of the ALD cycle ratio added (Figure S3, Supporting Information). From the comparison of the different films (Table S2, Supporting Information), we observed an increase in the height ratio of N-LO: LO from 27% to 40%, and then to 76% as the ALD cycle ratio of ZnO in the RS layer increases, correlating to the electrical behavior. In this work, the RS layer with an ALD cycle ratio of 1:1 exhibits the best performance.

From previous works, it is widely agreed the switching mechanism of metal-oxides like HfO_x is typical of filament formation via oxygen vacancies when no diffusing electrodes (e.g., Ag) are used.[45] And the Ti layer adjacent to the metal oxide often acts as an oxygen getter that helps to generate the oxygen vacancies for switching.[48,49] To prove the switching mechanism, 4 types of HfZnO RRAMs with the sizes of 3×3 µm^2, 5×5 µm^2, 10×10 µm^2, and 15×15 µm^2 were used. For each size, the LRS of 30 devices was measured to account for the impact of device-to-device variation. No area dependence was observed, as shown in Figure S4 (Supporting Information), thus, suggesting a filamentary mechanism of HfZnO RRAM.

In addition to the better DC electrical characteristics, the HfZnO RRAM shows lower switching current and faster switching speed as well as lower switching energy than HfO_x RRAM from AC pulse measurements. The switching speeds of the HfO_x and HfZnO RRAM are shown in Figure 3e–h. For a consistent comparison, the same set/reset voltage pulses (blue) with a pulse width of 1 µs were applied to both RRAMs, with corresponding response current (red). Read operations before and after the set/reset pulses are used to verify the validity of the switching. The switching speeds of two types of RRAMs are defined as the latency between the set pulse and response current. From Figure 3e,g, it can be clearly seen that both of RRAMs present a normal switching process under the pulse condition and that the read current increases after the set pulse and decreases after the reset pulse. The switching speeds of the HfO_x and HfZnO RRAM can be observed from the zoom-in image in Figure 3f,h, which are extracted to be 50 and 30 ns, respectively. In addition, the HfZnO RRAM switches with a lower response current (1.03 mA vs. 0.57 mA) under the same set pulses, resulting in a 3× reduction in switching energy down to 19 pJ.

The HfZnO RRAM also exhibits good stability which is presented in both retention endurance. The retention behaviors of the HfZnO RRAM were measured at various elevated temperatures (150 °C, 175 °C, 200 °C, 210 °C) until the time to failure (TTF), which is defined as the time point when resistance state of the device changes from LRS to HRS, as shown in Figure S5 (Supporting Information). Utilizing the TTF presented in Figure S5 (Supporting Information), the corresponding Arrhenius plot is plotted out, as shown in **Figure 4**a.[50,51] Thereafter, via extrapolating to room temperature, we show that the HfZnO RRAM can achieve a retention time exceeding 10 years. The write/erase endurance was also measured by applying a positive pulse (1.75 V/50 ns) to the device followed by a negative pulse (–2.25 V/60 ns) to perform a complete write/erase cycle. Figure S6 (Supporting Information) shows the first 300 continuous write/erase cycles under the same set/reset pulse with an ON/OFF ratio >1 order. Figure 4b shows the ON/OFF ratio of the device remained stable at >1 order even after more than 10^5 switching cycles were performed.

Table 1 compares the HfZnO RRAM with various reported oxide-based RRAM, including RRAMs based on Li_xSiO_y, 2D material oxide double-layer (2DMOD), nanocrystals (NC)-HfO_x, TiO_x-NiSi, and Anodic TiO_{2-x}.[26,52–55] Benefitting from the smaller switching voltage and corresponding current, the switching energy of the HfZnO RRAM (≈19 pJ) is much lower than the other reported RRAMs shown in the table.

For the characterization of the analog properties, both DC sweep and pulse were applied to the HfZnO RRAM. **Figure 5**a shows different states of the device, which were modulated by changing the stop voltage (SV) of the DC reset sweep, and with read voltage (V_{read}) sweeping from 0 to 0.2 V. In addition, Figure 5b also exhibits multiple conductance states under pulsed conditions. The potentiation (P) and depression (D) are described as modulated increase and decrease in conductance during the pulsing operations.[11,56,57] However, a complete switching to low/high conductance might happen if pulse

© 2023 The Authors. Advanced Electronic Materials published by Wiley-VCH GmbH

2199160x, 2023, 3, Downloaded from https://onlinelibrary.wiley.com/doi/10.1002/aelm.202201250 by University of Hong Kong, Wiley Online Library on [26/12/2023]. See the Terms and Conditions (https://onlinelibrary.wiley.com/terms-and-conditions) on Wiley Online Library for rules of use; OA articles are governed by the applicable Creative Commons License

ADVANCED ELECTRONIC MATERIALS Open Access
www.advelectronicmat.de

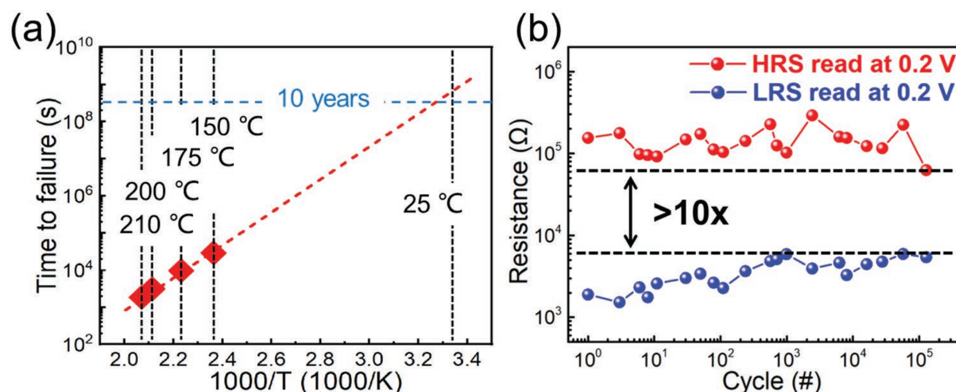

Figure 4. a) Arrhenius plot of data retention. b) Endurance measurement of the HfZnO RRAM with an ON/OFF ratio maintaining 1 order after more than 10^5 cycles of write/erase operations.

signals were applied with inappropriate width or amplitude, which may also lead to irreversible damage to the device. To avoid this situation, we tried different pulse conditions and chose pulses with appropriate width and amplitude (P: 0.9 V/1 µs, D: –1 V/1 µs) to measure the multi-states characteristics of the device. Figure 5b shows the P/D cycles of the device under 50 identical pulses respectively, while the thick fitted curve (red) with standard deviation for 5 consecutive P/D cycles shows variation for precise states tuning. This indicates that the multiple states modulation of the device has good repeatability. Based on the extracted programming characteristic, we employed NeuroSim to evaluate the offline learning/online classification of the mixed national institute of standards and technology (MNIST) handwriting recognition database.[8] As shown in Figure 5c, a two-layer multiplayer perceptron (MLP) neural network model with 400 input neurons, 100 hidden neurons, and 10 output neurons was utilized. The 400 input neurons correspond to a downscaled 20 × 20 MNIST data, and the 10 output neurons correspond to 10 classes of digits (0–9). In this simulation, the recognition training accuracy can reach ≈90% as shown in Figure 5d. It is worth mentioning that the accuracy could be further improved by optimizing the weight tuning schemes of increasing analog states, as well as device structure engineering to achieve a higher non-linearity factor.[58] Nonetheless, the initial results prove the potential of our RRAM as an analog memory and provide a pathway to achieve better performance.

The HfZnO RRAM also exhibits functional switching characteristics at the temperature down to 4 K. As reported in many works that RRAM shows normal switching behavior under cryogenic conditions,[13–15] we measured characteristics of the HfZnO RRAM under cryogenic conditions. 20 cycles of switching were measured and the average curves are plotted out in **Figure 6**a. The related switching characteristics of HfO_x RRAM were also measured and plotted in Figure S7 (Supporting Information). Here, we define V_{sw} as the threshold voltage at which switching occurs. The V_{sw} extracted from Figure 6a was plotted out in Figure 6b. It can be observed in Figure 6b that V_{sw} of the HfZnO RRAM shows a slight decreasing trend with increasing temperature as guided by the fitted dashed line, consistent with the observation from measured HfO_x RRAM (Figure S7, Supporting Information) and previously reported work.[14] However, the V_{sw} of the HfZnO RRAM is more scattered and insensitive to temperature, thus suggesting that the HfZnO RRAM is more temperature independent. It is agreed that the switching process of RRAM originates from the separation and recombination of oxygen vacancies and anions under the combined effects of electric field and Joule heating.[59,60] Joule heating can alleviate the effect of ambient temperature, for the local temperature generated from Joule heating is generally larger than the ambient temperature.[60–63] For the HfZnO RRAM, the slight increase of V_{sw} proves that the switching process does suffer from the lack of energy under cryogenic conditions so that larger voltage is needed to ensure the switching. However, Joule heating might be exacerbated by the introduction of the Zn element and, thus, alleviates the effect of ambient temperature on the switching process of HfZnO RRAM.

In order to get a better understanding of the behavior of our fabricated RRAM over the entire temperature range measured, the temperature dependence of devices' resistance (under a V_{read}

Table 1. Performance benchmarks of reported RRAMs.

Ref	RS layer/Thickness [nm]	V_{Form} [V]	$V_{set/reset}$ (DC)[V]	Energy [J]	Retention [s]
[26]	Li_xSiO_y/15	2.8	1/–1	≈62.5p	>10^3 s@280 °C
[52]	2DMOD/100	0.5	0.16/0.06	≈30p	>4 × 10^4 s @RT
[53]	NC-HfO_x/17	5.2	1.2/–1.05	≈800p	>10^4 s@85 °C
[54]	TiO_x-NiSi/10	4.37	2.34/–1.61	≈400p	>10^4 s@85 °C
[55]	Anodic TiO_{2-x}/10	1.4	0.8/–0.8	1.35n	NA
This work	HfZnO/5	1.77	0.95/–1.06	≈19p	>10 years @RT

© 2023 The Authors. Advanced Electronic Materials published by Wiley-VCH GmbH

2199160x, 2023, 3, Downloaded from https://onlinelibrary.wiley.com/doi/10.1002/aelm.202201250 by University of Hong Kong, Wiley Online Library on [26/12/2023]. See the Terms and Conditions (https://onlinelibrary.wiley.com/terms-and-conditions) on Wiley Online Library for rules of use; OA articles are governed by the applicable Creative Commons License

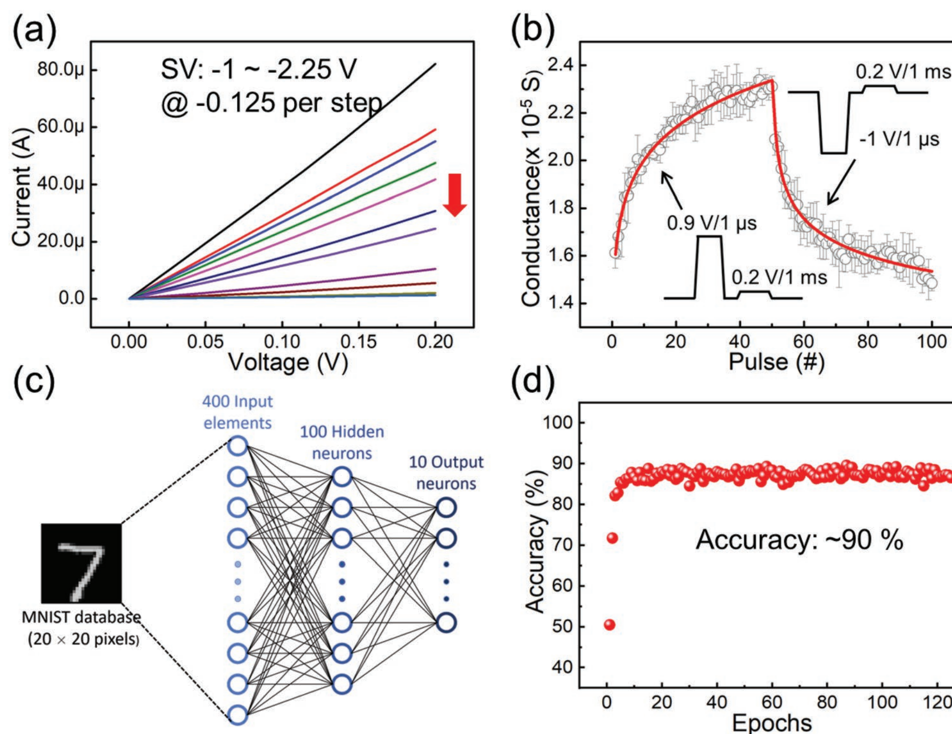

Figure 5. a) Multiple states modulated by changing SV with a step of −0.125 V, and b) standard deviation and fitting curve of 5 conductance modulation cycles with 50 identical positive voltage pulses for potentiation and 50 identical negative voltage pulses for depression. c) Schematic of two-layer MLP neural network for MINIST handwriting (0 to 9) recognition and d) simulated accuracy in determining handwritten patterns.

of 0.2 V) is plotted in Figure S8 (Supporting Information). It is observed that the resistance of HRS slightly decreases with the increasing of temperature at a temperature lower than 77 K and decreases faster when the temperature exceeds 77 K. This phenomenon is consistent with reported works,[14] which indicates a hopping mechanism. However, the temperature-dependent LRS of the HfZnO RRAM shows a different trend, that is, the resistance decreases very slowly to a minimum point, and starts to increase above 77 K. It is hence suggested that two different transport mechanisms are at play. For a deeper analysis of the mechanisms, the resistances plotted in Figure S8 (Supporting Information) were separated according to resistance states and temperature range, as shown in Figure 6c–f. Figure 6c,d shows the plot of ln(σ) versus $T^{-1/4}$ and ln(σ) versus T^{-1} for the HRS of HfZnO RRAM, respectively. It can be inferred that the electron hopping mechanism is dominant with increasing resistance at a lower temperature that eventually saturates. Electrons are transported through nearest neighboring hopping (NNH) at high temperatures (follows T^{-1} law), and transfer to a variable range hopping (VRH) mechanism at lower temperatures. It is also indicated by the extracted energy barrier from both regions (See Table S3, Supporting Information), in which the energy barrier in the region above 77 K is higher than that below 77 K. It indicates that electrons in the region above 77 K could obtain sufficient thermal energy to hop to the nearest trap, that is, the NNH. However, in the region at a lower temperature (below 77 K), electrons could only seek for a longer hopping path to the farther traps but with a lower energy barrier height, that is, the average hopping length is larger, due to the lack of thermal energy.[14,64] Given that the hopping transport happens at a very low barrier height of 0.2 meV (See Table S3, Supporting Information), it is reasonable that electrons are easier to hop to the traps with longer hopping paths. Hence, the conduction mechanism transits to the VRH mechanism. A similar type of small polaron hopping has been proved to exhibit the same transition of slope by Wang et al.,[65] in which the transition temperature is about half of the Debye temperature because polarons will be frozen out at lower temperatures. Meanwhile, it should be noted that, as indicated in XPS, the Zn-doped HfO_x film have a high density of defects, which may lead to a lower barrier height, suitable for cryogenic operation. This might be helpful for the electrons to hop to the traps at a longer path (i.e., larger average hopping length) at low temperatures.

For the LRS, on the one hand, as shown in Figure 6e, the decrease of resistance with temperature can also be explained by the VRH mechanism, where the measured conductivity follows the $T^{-1/4}$ law.[66] This is further supported by Mott's theory, where the phenomenon of VRH is always observed when the temperature is close to zero. On the other hand, the increase of resistance with temperature supports the metallic conduction mechanism (Figure 6f) with Equation (1)[64,67]

$$R(T) = R_0\left[1+\beta(T-T_0)\right] \tag{1}$$

where R_0 is the resistance at a temperature of T_0 and β is the temperature coefficient. As compared to former reported works of HfO_x,[14] it is worth pointing out that the incorporation of Zn may affect the LRS, which can be further supported by the larger number of defects as characterized by XPS, resulting in the transition from hopping conduction to partial metallic conduction. Works based on HfO_{2-x} RRAM considering impurity in

© 2023 The Authors. Advanced Electronic Materials published by Wiley-VCH GmbH

2199160x, 2023, 3, Downloaded from https://onlinelibrary.wiley.com/doi/10.1002/aelm.202201250 by University of Hong Kong, Wiley Online Library on [26/12/2023]. See the Terms and Conditions (https://onlinelibrary.wiley.com/terms-and-conditions) on Wiley Online Library for rules of use; OA articles are governed by the applicable Creative Commons License

ADVANCED ELECTRONIC MATERIALS
Open Access
www.advelectronicmat.de

2199160x, 2023, 3, Downloaded from https://onlinelibrary.wiley.com/doi/10.1002/aelm.202201250 by University of Hong Kong, Wiley Online Library on [26/12/2023]. See the Terms and Conditions (https://onlinelibrary.wiley.com/terms-and-conditions) on Wiley Online Library for rules of use; OA articles are governed by the applicable Creative Commons License

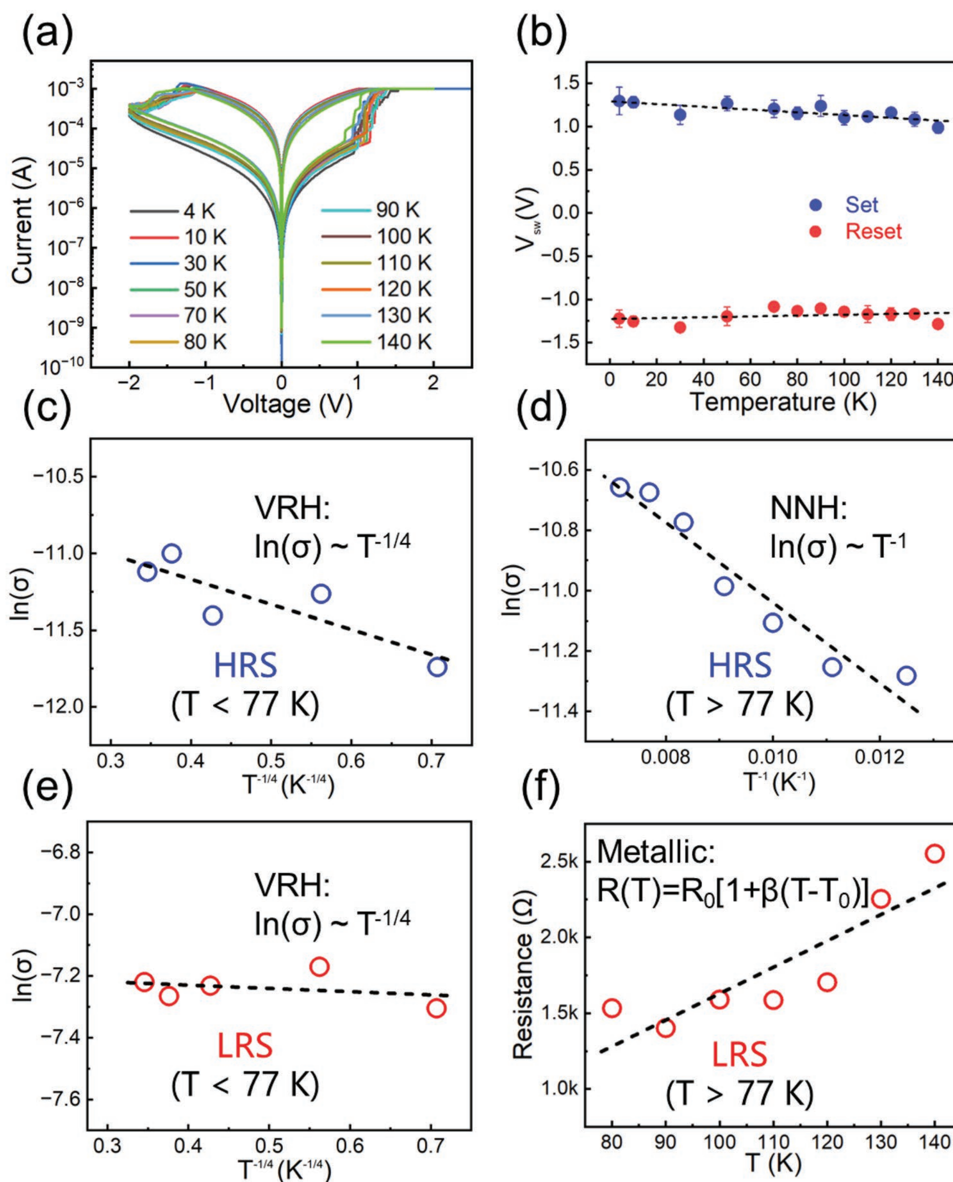

Figure 6. a) I–V curve of HfZnO RRAM at low temperature (4–140 K), and b) temperature dependence of switching voltage for the set/reset process. c) VRH and d) NNH fitting for HRS below and above 77 K, e) VRH fitting for LRS below 77 K, and f) its temperature dependence above 77 K.

the RS layer have suggested that the Ohmic charge transport in the LRS can be caused by the formation of a metallic subband due to high oxygen defects concentration.[65] A similar phenomenon was also reported in some mixed metal oxides.[68]

3. Conclusion

In summary, we present a HfZnO RRAM prepared via a low-temperature ALD process with enhanced performance. As compared to HfO_x RRAM, the HfZnO RRAM boasts a smaller and tighter operating voltage (1.77/0.95/–1.05 V) and lower switching energy (19 pJ) due to the larger content of defects from Zn doping. Through systematic electrical characterizations, we show that the HfZnO RRAM also exhibits excellent retention, repeatability, and multi-states tuning characteristics, resulting in a ≈90% simulated MLP accuracy for MNIST handwriting recognition. Finally, the HfZnO RRAM can still switch normally under cryogenic conditions (down to 4 K), and the conduction mechanism was investigated. Our results provide a feasible avenue to engineer high-performance RRAM in a controllable manner, for various emerging applications such as in-memory-computing, and cryogenic circuitries for quantum computing, deep-space exploration, etc.

4. Experimental Section

Device Fabrication: Both HfO_x-based control RRAM and HfZnO RRAM were fabricated on a 285 nm-SiO_2-capped Si substrate. The bottom electrode (BE) composed of Ti (5 nm)/Pt (20 nm) was first

 © 2023 The Authors. Advanced Electronic Materials published by Wiley-VCH GmbH

ADVANCED ELECTRONIC MATERIALS
Open Access
www.advelectronicmat.de

formed using lithography and deposited using an e-beam evaporator. After the lift-off process, an O_2 plasma process was used to remove the photoresist residues. After that, RS layers were prepared using Picosun thermal ALD system with trimethylgallium (TMG) precursor for Hf, and diethylzinc (DEZ) for Zn. H_2O was used as the oxygen reactant. Four RS layers with ALD cycle ratios (ZnO: HfO_2) of 0:1, 1:1, 1:3, and 1:0 were prepared, with all having a thickness ≈5 nm. For each type of film, different number of layers was alternatively deposited, which contain sublayers corresponding to ALD cycle ratios (ZnO: HfO_2). RS layers with ALD cycle ratios (ZnO: HfO_2) of 0:1 and 1:0, that is HfO_x layer and ZnO layer were directly deposited by 50 cycles of HfO_2 and ZnO, respectively. RS layer with ALD cycle ratios (ZnO: HfO_2) of 1:1, that is HfZnO layer, contains 25 alternative layers, all of which are composed of 1 cycle of ZnO and 1 cycle of HfO_2. For the RS layer with ALD cycle ratios (ZnO: HfO_2) of 1:3, 13 alternative layers were deposited containing 3 cycles of ZnO and 1 cycle of HfO_2 in each layer. Finally, the top electrode of Ti (8 nm)/Pt (20 nm) was deposited using an e-beam evaporator. Devices with the cell size of $3 \times 3\ \mu m^2$, $5 \times 5\ \mu m^2$, $10 \times 10\ \mu m^2$, and $15 \times 15\ \mu m^2$ were fabricated, in which device with a cell size of $5 \times 5\ \mu m^2$ was used for normal measurement.

Characterizations: Electrical characteristics were measured using a Keysight B1500A semiconductor parameter analyzer and Everbeing C-4 probe station, while the low-temperature measurements were conducted using a Lakeshore cryogenic probe station. Voltage bias was applied to the TE with BE grounded. The TEM was performed with a Thermo Fisher Talos F200X G2. The AFM images were obtained by Dimension Edge. XPS analysis was performed by EscaLab 250Xi of Thermo Fisher Scientific with a monochromatic Al Kα X-ray source (hν = 1486.6 eV). All the measured films with a thickness of ≈5 nm were deposited on the pure Si wafer under the totally same conditions as the corresponding device. XPS data were analyzed using Thermo Avantage software. All binding energy data were calibrated by the C 1s signal from surface-adsorbed hydrocarbon at 284.8 eV. High-resolution spectra with a step size of 0.1 eV were recorded for each peak.

Supporting Information

Supporting Information is available from the Wiley Online Library or from the author.

Acknowledgements

J.L. and Z.L. contributed equally to this work. This work was supported by the National Natural Science Foundation of China (Grant No. 62174074, 62274081, 62104091, 52273246), Guangdong Young Innovative Talent Project Research Program (Grant No. 2021KQNCX077), Shenzhen Fundamental Research Program (Grant No. JCYJ20220530115014032, JCYJ20220530115204009, JCYJ20190809143419448), Special Funds for the Cultivation of Guangdong College Students' Scientific and Technological Innovation (Grant pdjh2023c11507, pdjh2022b0455), SUSTech SME-Pixelcore Neuromorphic In-sensor Computing Joint Lab and Guangdong Provincial Engineering Research Center of 3-D Integration. The authors would also like to acknowledge the Core Research Facilities (CRF) at SUSTech for the facilities used, and the technical support provided by the staff and engineers at the CRF.

Conflict of Interest

The authors declare no conflict of interest.

Data Availability Statement

The data that support the findings of this study are available from the corresponding author upon reasonable request.

Keywords

4 K, cryogenic, hafnium oxide, resistive switching, resistive random-access memory (RRAM), zinc

Received: November 21, 2022
Revised: January 10, 2023
Published online: January 29, 2023

[1] H.-Y. Chen, S. Brivio, C.-C. Chang, J. Frascaroli, T.-H. Hou, B. Hudec, M. Liu, H. Lv, G. Molas, J. Sohn, S. Spiga, V. M. Teja, E. Vianello, H. S. P. Wong, *J. Electroceram.* **2017**, *39*, 21.
[2] H. Wu, X. H. Wang, B. Gao, N. Deng, Z. Lu, B. Haukness, G. Bronner, H. Qian, *Proc. IEEE* **2017**, *105*, 1770.
[3] H. S. P. Wong, H.-Y. Lee, S. Yu, Y.-S. Chen, Y. Wu, P.-S. Chen, B. Lee, F. T. Chen, M.-J. Tsai, *Proc. IEEE* **2012**, *100*, 1951.
[4] X. Feng, Y. Li, L. Wang, S. Chen, Z. G. Yu, W. C. Tan, N. Macadam, G. Hu, L. Huang, L. Chen, X. Gong, D. Chi, T. Hasan, A. V. Y. Thean, Y. W. Zhang, K. W. Ang, *Adv. Electron. Mater.* **2019**, *5*, 1.
[5] Y. Li, X. Feng, M. Sivan, J. F. Leong, B. Tang, X. Wang, J. N. Tey, J. Wei, K. W. Ang, A. V. Y. Thean, *IEEE Sens. J.* **2020**, *20*, 4653.
[6] B. Tang, H. Veluri, Y. Li, Z. G. Yu, M. Waqar, J. F. Leong, M. Sivan, E. Zamburg, Y. W. Zhang, J. Wang, A. V. Thean, *Nat. Commun.* **2022**, *13*, 3037.
[7] C. Li, D. Belkin, Y. Li, P. Yan, M. Hu, N. Ge, H. Jiang, E. Montgomery, P. Lin, Z. Wang, W. Song, J. P. Strachan, M. Barnell, Q. Wu, R. S. Williams, J. J. Yang, Q. Xia, *Nat. Commun.* **2018**, *9*, 2385.
[8] P.-Y. Chen, X. Peng, S. Yu, presented at *2017 IEEE Int. Electron Devices Meeting*, XX, San Francisco, USA December **2017**.
[9] M. Zaheer, A. U. Bacha, I. Nabi, J. Lan, W. Wang, M. Shen, K. Chen, G. Zhang, F. Zhou, L. Lin, M. Irshad, F. Faridullah, A. Arifeen, Y. Li, *ACS Omega* **2022**, *7*, 40911.
[10] H. Veluri, Y. Li, J. X. Niu, E. Zamburg, A. V.-Y. Thean, *IEEE Internet Things J.* **2021**, *8*, 9219.
[11] Y. Xi, B. Gao, J. Tang, A. Chen, M.-F. Chang, X. S. Hu, J. V. D. Spiegel, H. Qian, H. Wu, *Proc. IEEE* **2021**, *109*, 14.
[12] J. Shang, G. Liu, H. Yang, X. Zhu, X. Chen, H. Tan, B. Hu, L. Pan, W. Xue, R.-W. Li, *Adv. Funct. Mater.* **2014**, *24*, 2171.
[13] Z. Hao, B. Gao, M. Xu, Q. Hu, W. Zhang, X. Li, F. Sun, J. Tang, H. Qian, H. Wu, *IEEE Electron Device Lett.* **2021**, *42*, 1276.
[14] R. Fang, W. Chen, L. Gao, W. Yu, S. Yu, *IEEE Electron Device Lett.* **2015**, *36*, 567.
[15] C. Vaca, M. B. Gonzalez, H. Castan, H. Garcia, S. Duenas, F. Campabadal, E. Miranda, L. A. Bailon, *IEEE Trans. Electron Devices* **2016**, *63*, 1877.
[16] F. Ware, L. Gopalakrishnan, E. Linstadt, S. A. McKee, T. Vogelsang, K. L. Wright, C. Hampel, G. Bronner, in *Proc. Int. Symp. Memory Systems*, Association for Computing Machinery, New York, USA **2017**, 183.
[17] P. Wang, A. I. Khan, S. Yu, *Appl. Phys. Lett.* **2020**, *116*, 162108.
[18] H. Chen, L. Li, J. Wang, G. Zhao, Y. Li, J. Lan, B. K. Tay, G. Zhong, J. Li, M. Huang, *IEEE Electron Device Lett.* **2022**, *43*, 1141.
[19] Y. Zhang, G. Q. Mao, X. Zhao, Y. Li, M. Zhang, Z. Wu, W. Wu, H. Sun, Y. Guo, L. Wang, X. Zhang, Q. Liu, H. Lv, K. H. Xue, G. Xu, X. Miao, S. Long, M. Liu, *Nat. Commun.* **2021**, *12*, 7232.
[20] Y. Fang, Z. Yu, Z. Wang, T. Zhang, Y. Yang, Y. Cai, R. Huang, *IEEE Electron Device Lett.* **2018**, *39*, 819.
[21] B. Magyari-Köpe, Y. Song, D. Duncan, L. Zhao, Y. Nishi, *APL Mater.* **2018**, *6*, 058102.
[22] L. Zhao, S.-W. Ryu, A. Hazeghi, D. Duncan, B. Magyari-Köpe, Y. Nishi, presented at *2013 Symp. VLSI Tech.* , XX, Kyoto, Japan June **2013**.
[23] Z. Wang, W. Zhu, A. Du, L. Wu, Z. Fang, X. A. Tran, W. Liu, K. Zhang, H.-Y. Yu, *IEEE Trans. Electron Devices* **2012**, *59*, 1203.

 © 2023 The Authors. Advanced Electronic Materials published by Wiley-VCH GmbH

2199160x, 2023, 3, Downloaded from https://onlinelibrary.wiley.com/doi/10.1002/aelm.202201250 by University of Hong Kong, Wiley Online Library on [26/12/2023]. See the Terms and Conditions (https://onlinelibrary.wiley.com/terms-and-conditions) on Wiley Online Library for rules of use; OA articles are governed by the applicable Creative Commons License

[24] M. Lübben, F. Cüppers, J. Mohr, M. von Witzleben, U. Breuer, R. Waser, C. Neumann, I. Valov, *Sci. Adv.* **2020**, *6*, aaz9079.
[25] N. Raeis-Hosseini, S. Chen, C. Papavassiliou, I. Valov, *RSC Adv.* **2022**, *12*, 14235.
[26] X. Zhao, X. Zhang, D. Shang, Z. Wu, X. Xiao, R. Chen, C. Tang, J. Liu, W. Li, H. Lv, C. Jiang, Q. Liu, M. Liu, *IEEE Electron Device Lett.* **2019**, *40*, 554.
[27] S. A. Khan, S. Kim, *RSC Adv.* **2020**, *10*, 31342.
[28] G. Vinuesa, O. G. Ossorio, H. García, B. Sahelices, H. Castán, S. Dueñas, M. Kull, A. Tarre, T. Jogiaas, A. Tamm, A. Kasikov, K. Kukli, *Solid-State Electron.* **2021**, *183*, 108085.
[29] M. Ismail, C. Mahata, O. Kwon, S. Kim, *ACS Appl. Electron. Mater.* **2022**, *4*, 1288.
[30] L. Zhang, H. Huang, C. Ye, K.-C. Chang, R. Zhang, Q. Xia, X. Wei, W. Wei, W. Wang, *Semicond. Sci. Technol.* **2018**, *33*, 085013.
[31] F. Wang, X. Zhao, L. Duan, Y. Wang, H. Niu, A. Ali, *J. Alloys Compd.* **2015**, *623*, 290.
[32] C. H. Ahn, J. H. Kim, H. K. Cho, *J. Electrochem. Soc.* **2012**, *159*, H384.
[33] T. Tynell, M. Karppinen, *Semicond. Sci. Technol.* **2014**, *29*, 043001.
[34] Y. P. Wang, W. I. Lee, T. Y. Tseng, *Appl. Phys. Lett.* **1996**, *69*, 1807.
[35] A. Janotti, C. G. Van de Walle, *Phys. Rev. B* **2007**, *76*, 165202.
[36] M. U. Khan, C. M. Furqan, J. Kim, S. A. Khan, Q. M. Saqib, M. Y. Chougale, R. A. Shaukat, M. H. Kang, N. P. Kobayashi, J. Bae, H.-S. Kwok, *ACS Appl. Electron. Mater.* **2022**, *4*, 297.
[37] X. Li, J. G. Yang, H. P. Ma, Y. H. Liu, Z. G. Ji, W. Huang, X. Ou, D. W. Zhang, H. L. Lu, *ACS Appl. Mater. Interfaces* **2020**, *12*, 30538.
[38] X. Li, Y. Wang, W. Liu, G. Jiang, C. Zhu, *Mater. Lett.* **2012**, *85*, 25.
[39] J. C. C. Fan, J. B. Goodenough, *J. Appl. Phys.* **1977**, *48*, 3524.
[40] J.-C. Dupin, D. Gonbeau, P. Vinatier, A. Levasseur, *Phys. Chem. Chem. Phys.* **2000**, *2*, 1319.
[41] M. Lübben, S. Wiefels, R. Waser, I. Valov, *Adv. Electron. Mater.* **2018**, *4*, 1700458.
[42] G. Milano, M. Luebben, M. Laurenti, L. Boarino, C. Ricciardi, I. Valov, *Adv. Mater. Interfaces* **2021**, *8*, 2100915.
[43] G. Milano, M. Luebben, M. Laurenti, S. Porro, K. Bejtka, S. Bianco, U. Breuer, L. Boarino, I. Valov, C. Ricciardi, *Adv. Mater. Interfaces* **2019**, *6*, 1900803.
[44] G. Milano, F. Raffone, M. Luebben, L. Boarino, G. Cicero, I. Valov, C. Ricciardi, *ACS Appl. Mater. Interfaces* **2020**, *12*, 48773.
[45] F. Zahoor, T. Z. Azni Zulkifli, F. A. Khanday, *Nanoscale Res. Lett.* **2020**, *15*, 90.
[46] M. Sivan, Y. Li, H. Veluri, Y. Zhao, B. Tang, X. Wang, E. Zamburg, J. F. Leong, J. X. Niu, U. Chand, A. V. Thean, *Nat. Commun.* **2019**, *10*, 5201.
[47] A. Bricalli, E. Ambrosi, M. Laudato, M. Maestro, R. Rodriguez, D. Ielmini, presented at *2016 IEEE Int. Electron Devices Meeting*, XX, San Francisco, CA December **2016**.
[48] S.-Y. Wang, D.-Y. Lee, T.-Y. Tseng, C.-Y. Lin, *Appl. Phys. Lett.* **2009**, *95*, 112904.
[49] C. Cagli, J. Buckley, V. Jousseaume, T. Cabout, A. Salaun, H. Grampeix, J. Nodin, H. Feldis, A. Persico, J. Cluzel, presented at *2011 Int. Electron Devices Meeting*, Washington, DC, USA July **2011**.
[50] M. Lanza, H. S. P. Wong, E. Pop, D. Ielmini, D. Strukov, B. C. Regan, L. Larcher, M. A. Villena, J. J. Yang, L. Goux, A. Belmonte, Y. Yang, F. M. Puglisi, J. Kang, B. Magyari-Köpe, E. Yalon, A. Kenyon, M. Buckwell, A. Mehonic, A. Shluger, H. Li, T.-H. Hou, B. Hudec, D. Akinwande, R. Ge, S. Ambrogio, J. B. Roldan, E. Miranda, J. Suñe, K. L. Pey, et al., *Adv. Electron. Mater.* **2019**, *5*, 1800143.
[51] Z. Wei, T. Takagi, Y. Kanzawa, Y. Katoh, T. Ninomiya, K. Kawai, S. Muraoka, S. Mitani, K. Katayama, S. Fujii, R. Miyanaga, Y. Kawashima, T. Mikawa, K. Shimakawa, k. Aono, presented at *2011 Int. Electron Devices Meeting*, XX, Washington, DC, USA December **2011**.
[52] X. Yan, C. Qin, C. Lu, J. Zhao, R. Zhao, D. Ren, Z. Zhou, H. Wang, J. Wang, L. Zhang, X. Li, Y. Pei, G. Wang, Q. Zhao, K. Wang, Z. Xiao, H. Li, *ACS Appl. Mater. Interfaces* **2019**, *11*, 48029.
[53] Q. Wu, W. Banerjee, J. Cao, Z. Ji, L. Li, M. Liu, *Appl. Phys. Lett.* **2018**, *113*, 023105.
[54] D. K. Lee, M.-H. Kim, S. Bang, T.-H. Kim, Y.-J. Choi, K. Hong, S. Kim, S. Cho, J.-H. Lee, B.-G. Park, *IEEE Trans. Electron Devices* **2021**, *68*, 438.
[55] S. Chen, S. Noori, M. A. Villena, Y. Shi, T. Han, Y. Zuo, M. Pedeferri, D. Strukov, M. Lanza, M. V. Diamanti, *Chem. Mater.* **2019**, *31*, 8394.
[56] N. Ilyas, C. Li, J. Wang, X. Jiang, H. Fu, F. Liu, D. Gu, Y. Jiang, W. Li, *J. Phys. Chem. Lett.* **2022**, *13*, 884.
[57] Z. Wang, M. Yin, T. Zhang, Y. Cai, Y. Wang, Y. Yang, R. Huang, *Nanoscale* **2016**, *8*, 14015.
[58] S. H. Foulger, Y. Bandera, B. Grant, J. Vilčáková, P. Sáha, *J. Mater. Chem. C* **2021**, *9*, 8975.
[59] Z. Peng, Y. Li, S. Qing-Qing, C. Lin, D. Shi-Jin, J. An-Quan, D. W. Zhang, *IEEE Trans. Nanotechnol.* **2012**, *11*, 1059.
[60] M. Uenuma, Y. Ishikawa, Y. Uraoka, *Appl. Phys. Lett.* **2015**, *107*, 073503.
[61] N. C. Das, M. Kim, J. R. Rani, S. M. Hong, J. H. Jang, *Nanoscale* **2022**, *14*, 3738.
[62] N. C. Das, M. Kim, S. M. Hong, J. H. Jang, *Micromachines* **2022**, *13*, 604.
[63] A. B. K. Chen, *Degree Thesis*, University of Pennsylvania, August, **2011**.
[64] Y. Zhang, N. Deng, H. Wu, Z. Yu, J. Zhang, H. Qian, *Appl. Phys. Lett.* **2014**, *105*, 063508.
[65] Z. Wang, H. Yu, X. A. Tran, Z. Fang, J. Wang, H. Su, *Phys. Rev. B* **2012**, *85*, 195322.
[66] N. F. Mott, E. A. Davis, *Electronic processes in non-crystalline materials*, Oxford university press, Oxford **2012**.
[67] R. Shabna, P. M. Sarun, S. Vinu, U. Syamaprasad, *J. Alloys Compd.* **2009**, *481*, 797.
[68] A. Bid, A. Bora, A. K. Raychaudhuri, *Phys. Rev. B* **2006**, *74*, 079903.

© 2023 The Authors. Advanced Electronic Materials published by Wiley-VCH GmbH

2199160x, 2023, 3, Downloaded from https://onlinelibrary.wiley.com/doi/10.1002/aelm.202201250 by University of Hong Kong, Wiley Online Library on [26/12/2023]. See the Terms and Conditions (https://onlinelibrary.wiley.com/terms-and-conditions) on Wiley Online Library for rules of use; OA articles are governed by the applicable Creative Commons License